




Cite this: *RSC Adv.*, 2023, 13, 13985

Facile fabrication of hierarchical ultrathin Rh-based nanosheets for efficient hydrogen evolution†

Changhui Jin, Ruijing Fu, Longqiao Ran, Wenhui Wang, Fuxin Wang,  Dezhou Zheng, Qi Feng and Guangxia Wang *

Rational design of efficient and stable electrocatalysts for the hydrogen evolution reaction (HER) has attracted wide attention. Noble metal-based electrocatalysts with ultrathin structures and highly exposed active surfaces are essential to boost the HER performance, while the simple synthetic strategies remain challenging. Herein, we reported a facile urea-mediated method to synthesize hierarchical ultrathin Rh nanosheets (Rh NSs) without using toxic reducing agents and structure directing agents in the reaction. The hierarchical ultrathin nanosheet structure and grain boundary atoms endow Rh NSs with excellent HER activities, which only requires a lower overpotential of 39 mV in 0.5 M H₂SO₄ compared to the 80 mV of Rh nanoparticles (Rh NPs). Extending the synthesis method to alloys, hierarchical ultrathin RhNi nanosheets (RhNi NSs) can be also obtained. Benefiting from the optimization of electronic structure and abundant active surfaces, RhNi NSs only require an overpotential of 27 mV. This work provides a simple and promising method to construct ultrathin nanosheet electrocatalysts for highly active electrocatalytic performance.

Received 31st January 2023
Accepted 1st May 2023

DOI: 10.1039/d3ra00672g

rsc.li/rsc-advances

Introduction

It is imperative to develop a clean, renewable energy to solve the problems of environmental pollution and the energy crisis caused by fossil fuel consumption. Hydrogen (H₂) is considered as one of the most promising alternatives to traditional fossil fuels due to its high energy density, renewable nature and zero emissions.^{1–5} Currently, electrochemical water splitting is an ideal method to generate high purity hydrogen.^{6–10} However, a considerable overpotential is still required to overcome the high energy barrier to drive the hydrogen evolution reaction (HER). Highly active electrocatalysts are suitable to reduce the reaction barrier and achieve effective water splitting. At present, noble metals are the most active catalysts to promote H₂ evolution, such as Pt-based catalysts.^{11–15} Nevertheless, the wide application of Pt catalysts is limited by its scarcity and high price. Therefore, it is imperative to explore economical and efficient catalysts for water splitting.

Recently, rhodium (Rh)-based materials have been proved as efficient HER electrocatalysts with corrosion resistance and excellent electrocatalytic activities.^{16–23} However, as a member of noble metals, the commercialization of Rh is still hindered by the limited performance improvement and the high price. Great efforts have been made to further improve the electrochemical

activity and reduce the cost of catalysts. One of the effective methods is increasing the active sites of catalysts. Two-dimensional (2D) nanosheets have drawn wide attention in the field of electrocatalysis owing to the large surface area, unique electronic structure and atomic thickness, including HER,^{24–28} oxygen evolution reaction (OER),^{29–31} methanol oxidation reaction (MOR)^{32,33} and oxygen reduction reaction (ORR),^{34–37} *etc.* For example, Chen's group used formaldehyde (HCHO) as a reducing agent to achieve ultrathin RhCo nanosheets with 1.3 nm thickness by a two-step method, which exhibited higher activity and long-term stability for the OER and HER than RuO₂ and Pt nanoparticle electrocatalysts.³⁸ Zhang's group also used HCHO to successfully synthesize ultrathin Rh and Rh alloy nanosheets, and revealed outstanding catalytic activity toward the direct synthesis of indole.³⁹ Additionally, Cui and co-workers prepared RhPdH bimetallic nanosheets with carbon monoxide (CO) gas as a surface covering agent and reducing agent. RhPdH bimetallic showed a lower overpotential and better stability compared with commercial Pt/C catalysts for HER in alkaline media.⁴⁰ Guo's group obtained ultrathin PdMo bimetallic nanosheets with only 0.88 nm thickness by using molybdenum carbonyl (Mo(CO)₆). The mass activity of PdMo for ORR was 78 times and 327 times higher than that of commercial Pt/C and Pd/C catalysts, respectively.⁴¹ The activities of the electrocatalysts are highly related to their morphology of 2D. While, due to the lack of inherent thermodynamic dynamics for crystal growth, the successful preparations of ultrathin nanosheets mainly depend on the using of CO gas or some chemicals which can produce CO at high

School of Applied Physics and Materials, Wuyi University, Jiangmen 529020, China.
E-mail: wangguangxia1107@126.com

† Electronic supplementary information (ESI) available. See DOI: <https://doi.org/10.1039/d3ra00672g>



temperature such as metal carbonyl compounds and HCHO. However, it has a significant negative effect on the health and environment because of the toxicity of metal carbonyl compounds, HCHO and CO gas. Obviously, it is essential to develop a simple and environmentally friendly synthesis method of 2D nanomaterials for precious metal-based electrocatalysts.

In addition, increasing intrinsic activity of catalysts is another important method to design efficient catalysts. Alloying noble metals with transition metal M (*e.g.*, Ni, Cu, Fe) can not only enhance the electrochemical performance by tuning their electronic structure but also significantly reduce the cost of the catalysts. For instance, RuNi alloy exhibited remarkable electrocatalytic activity in alkaline HER due to the alloying effect with Ni, which can facilitate the dissociation of water and optimize the adsorption and desorption of hydrogen.⁴²

In this work, we obtained Rh-based nanosheets by a facile urea-mediated route for the first time, which could display superior electrochemical hydrogen evolution performance in acidic solution. Specifically, the ultrathin nanosheets assembled into hierarchical architecture, which can prevent the agglomeration of ultrathin nanostructures during the electrocatalytic process. Impressively, Rh NSs only requires an overpotential of 39 mV to achieve a current density of 10 mA cm⁻² in 0.5 M H₂SO₄. Extending the synthesis method to alloys, RhNi NSs were obtained to modulate the electronic structure of Rh, which exhibited superior electrochemical hydrogen evolution performance to the monometallic counterparts. We propose that the high specific surface area and grain boundary endow Rh NSs and RhNi NSs with excellent HER activities. Besides, the ultrathin nanosheets geometry has an intrinsic advantage in charge transport, which is also conducive to the more efficient utilization of noble metal electrocatalysts.

Experimental section

Materials

Rhodium(II) acetate dimer (C₈H₁₂O₈Rh₂), polyvinylpyrrolidone (PVP, *M_w* ≈ 55 000), rhodium(III) acetylacetonate (C₁₅H₂₁O₆Rh) and Ethylene glycol (EG) were obtained from Sigma-Aldrich Reagent Company. Nickel(II) acetate tetrahydrate (NiC₄H₆O₄·4H₂O) and urea were purchased from Shanghai Aladdin Reagent Co., Ltd. Benzyl alcohol (C₇H₈O) was purchased from Shanghai Macklin Reagent Co., Ltd. Nickel(II) acetylacetonate (C₁₀H₁₄NiO₄) was brought from Alfa Aesar Chemical Co., Ltd. All the chemicals were used as received without further purification.

Sample preparations

Rh ultrathin nanosheets were prepared *via* a solvothermal method. First, 60 mg of PVP was dissolved in 4 mL of EG solution and then the vial was heated at 160 °C for 10 min. Then, 10.38 mg of rhodium(II) acetate dimer and 0.8 g urea were dispersed in 2 mL EG after ultra-sonication. Then, the mixture was added to the above solution and reacted at 160 °C for 8 h. After cooling under ambient conditions, the product was

collected by centrifugation and washed with ethanol. RhNi NSs was synthesized under similar to those of Rh NSs, except that 5.84 mg Nickel(II) acetate tetrahydrate was added as the nickel source.

The Rh nanoparticles were prepared by a solvothermal method based on literature reports with slight modifications.^{43,44} Firstly, 8 mg rhodium(III) acetylacetonate and 120 mg PVP were added to the 6 mL benzyl alcohol solution. The solution was then vigorously stirred for 1 h to form a homogeneous solution, and then transferred to a Teflon-lined stainless steel autoclave. The vessel was sealed and heated at 180 °C for 8 h, and then naturally cooled to room temperature before the resulting products were collected by ethanol centrifugation. The RhNi nanoparticles were synthesized under similar conditions to that of the Rh NPs, except that 2.57 mg of nickel(II) acetylacetonate was added as the nickel source.

Characterizations

X-ray diffraction (XRD) patterns were conducted on a X'Pert3 Powder diffractometer equipped with Cu K α radiation (λ = 0.15405 nm). The operation voltage and current were 40 kV and 40 mA, respectively. Field emission scanning electron microscopy (SEM) was carried out on a Zeiss Sigma 500. The transmission electron microscopy (TEM) and high-resolution transmission electron microscopy (HRTEM) images were collected by using JEOL JEM-2100F. The X-ray photoelectron spectroscopy (XPS) characterization were obtained on a Thermo Scientific K-Alpha.

Electrochemical measurements

All electrochemical experiments were carried out at room temperature using a CHI-660E electrochemical workstation. HER tests were carried out in a 0.5 M H₂SO₄ electrolyte using a standard three-electrode system in which a catalyst-coated glassy carbon electrode (GCE, diameter: 5 mm, area: 0.196 cm²), a saturated calomel electrode and a carbon rod were used as working, reference and counter electrode respectively. The catalyst ink was prepared by mixing 1 mg of catalysts, 4 mg of carbon black (Vulcan XC-72), 2 mL of isopropyl alcohol and 100 μ L of Nafion solution (5 wt%). The mixture was sonicated for 1 h until a homogeneous ink formed. Then, 20 μ L of the ink solution was cast on the pretreated GCE and dried naturally at room temperature. The HER activity of the catalyst was assessed using linear sweep voltammetry (LSV), where the scan rate was 5 mV s⁻¹. All LSV polarization curves were corrected with iR compensation, where *i* is the current and *R* is the ohmic resistance of the electrolyte measured with electrochemical impedance spectroscopy (EIS). The electrochemical impedance spectroscopy (EIS) curves were tested in the frequency range 10 000 Hz to 1 Hz with an amplitude of 5 mV. The electrochemical double layer capacitance (*C_{dl}*) was performed by cyclic voltammetry (CV) at various scanning rates of 20, 40, 60, 80, 100 and 120 mV s⁻¹. The durability test of the catalyst was performed by chronopotentiometry (*V-t*) at a fixed current density of 10 mA cm⁻². All potentials in this study were calibrated by referring to the reversible hydrogen electrode (RHE), and the current



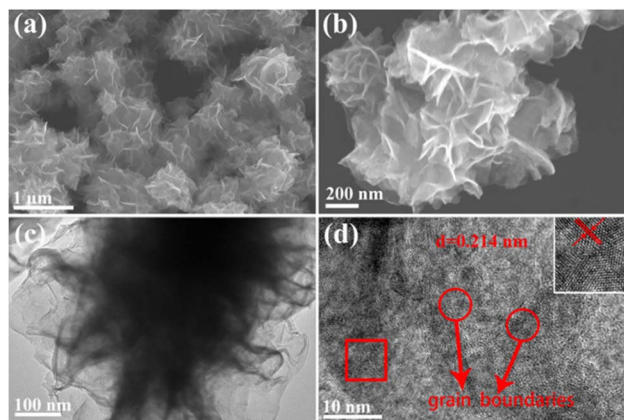


Fig. 1 (a and b) SEM images, (c) TEM image, and (d) HRTEM image of Rh NSs.

density was normalized by the geometric area of the glass carbon electrode.

Results and discussion

Material characterizations

Rh NSs were prepared by a simple one-step solvothermal synthesis. The morphology and structure of Rh NSs are illustrated in Fig. 1. The SEM images show that the sample has a hierarchical architecture assembled by ultrathin nanosheets. From the high-magnification SEM image in Fig. 1b, it is clearly found that the products have a rough surface. TEM image (Fig. 1c) further confirms that Rh NSs contain ultrathin nanosheets, consistent with SEM characterization. The lattice spacing of 0.214 nm is observed in the high-resolution TEM (HRTEM) image (Fig. 1d), corresponding to the (111) crystal plane of face-centered cubic (fcc) Rh. It is obviously observed that Rh possesses an ultrathin structure and grain boundary atoms.³³ The structure of Rh is expected to enhance the catalytic activity due to the large surface area which can provide more active sites. Besides, the crystallographic texture of Rh NSs was also investigated by XRD (Fig. 2). Three diffraction peaks of Rh NSs around 41.1°, 47.7°, and 69.9° are corresponded to the

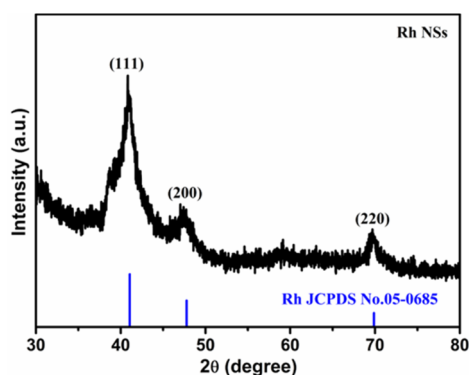


Fig. 2 XRD pattern of Rh NSs.

(111), (200), and (220) facet of the fcc Rh (JCPDS no. 05-0685) crystal, respectively.

In order to study the effect of synthesis conditions on the morphology of the products, a number of control experiments were carried out. The effect of PVP was investigated and the characterizations were shown in Fig. S1†. A similar nanosheet structure can be obtained without PVP, while the thickness is slightly thicker. Adjusting the reaction temperature to 140 °C, there is almost no precipitation after centrifugation. Raising the temperature to 180 °C, the morphology of ultrathin nanosheets can also be obtained (Fig. S2†). We also explored the reaction process. When the reaction continues for 0.5 h at 160 °C, the nanosheets skeleton appear (Fig. S3a†). After reacted for 4 h, nanosheets gradually become larger (Fig. S3b†). When the reaction time proceeded for 10 h, the nanosheets structure almost remains unchanged (Fig. S3c†) compared with that of 8 h (Fig. 1a). In addition, the amount of urea plays the most important role in the formation of 2D nanosheet. The SEM images of Rh were presented in Fig. S3d–f† with different amount of urea. As the amount of urea is excessive, the agglomerated clusters appear and the structure of nanosheet is broken. When tiny amount of urea added to the solution, no nanosheets are obtained. Therefore, it is inferred that urea acts as a structure directing agent in the reaction. After adding a proper amount of urea, smaller pieces will be generated rapidly at the initial stage of the reaction. And with the extension of the reaction time, the smaller sheets will grow further and become ultrathin nano-sheets.

To demonstrate the universality of the proposed urea-mediated synthetic method, bimetallic RhNi alloy nanosheet was successfully prepared by mixing rhodium(III) acetate dimer and nickel(II) acetate tetrahydrate precursors in the reaction solution. The structure of the obtained RhNi NSs is shown in Fig. 3. Similar to the morphology of Rh NSs, the RhNi NSs still exhibit the typical sheet-like structure and a rough surface. According to the elemental mappings of Fig. 3c, f, and i, the

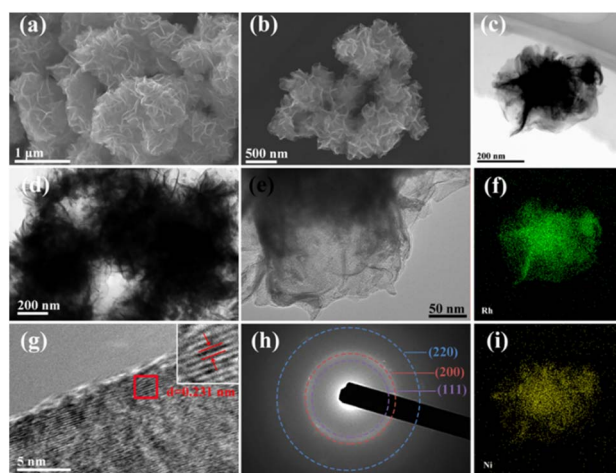


Fig. 3 (a and b) SEM images, (c) HAADF-STEM image, (d and e) TEM images, (f and i) EDS, (g) HRTEM image, and (h) SAED pattern of RhNi NSs.



elements Rh and Ni are homogeneously distributed in the RhNi NSs. The lattice spacing of 0.231 nm in HRTEM image (Fig. 3g) evidences a decrease in the interplanar spacing compared to the fcc Rh (111) crystal plane. The SAED pattern (Fig. 3h) shows RhNi NSs with multiple diffraction rings, confirming the polycrystalline structure of RhNi NSs. In addition, the XRD characterization of RhNi NSs was presented in Fig. S4a.† In comparison with monometallic Rh NSs, the peak of (111) slightly shifted to a higher angle, suggesting the incorporation of Ni into the crystal lattice of Rh. An additional shoulder peak near the main peaks evolves at about 38.5° , which may be originated from the oxidation of metallic Rh in air. These results indicate that the nanosheets synthetic method we proposed have successfully synthesized RhNi NSs with binary alloy structures.

The surface composition and chemical state of RhNi NSs were studied using X-ray photoelectron spectroscopy (XPS). The full-scan spectrum of the RhNi NSs (Fig. S4b†) demonstrates the presence of the Rh and Ni elements. The high-resolution Rh 3d XPS spectra (Fig. S4c†) shows that metallic Rh^0 and oxidized Rh^{3+} species co-exist in RhNi NSs. In particular, the Rh 3d XPS spectrum has two main peaks at 308 eV and 312.8 eV corresponding to the $3d_{5/2}$ and $3d_{3/2}$ peaks of the metallic Rh^0 .⁴⁵ The peaks around 310 eV and 314.8 eV correspond to the $3d_{5/2}$ and $3d_{3/2}$ peaks of Rh^{3+} species, respectively, which may result from the oxidized surficial Rh in air.^{46,47} The high-resolution Ni 2p XPS spectra shows peaks at 855.5 and 873.2 eV corresponding to the $2p_{3/2}$ and $2p_{1/2}$ peaks of the metallic Ni^0 .⁴⁸ Two peaks at 857.2 and 874.9 eV corresponding to the $2p_{3/2}$ and $2p_{1/2}$ peaks of Ni^{2+} species (Fig. S4d†). Obviously, the shift of binding energy of Rh^0 for RhNi NSs in comparison to Rh NSs suggests the electronic interactions between the Ni and Rh, which may optimize the adsorption energy of the intermediates.

Electrocatalytic performance

The HER activities of Rh NSs and RhNi NSs were evaluated at room temperature using a three-electrode system in 0.5 M H_2SO_4 . For comparison, the performance of Rh and RhNi with the morphology of particles (TEM and XRD images were shown in Fig. S5 and S6†) were also tested. Generally, the overpotential at the current density of 10 mA cm^{-2} is an important parameter to measure the HER performance of catalysts. As displayed in Fig. 4a and b, Rh NSs and RhNi NSs require overpotentials of 39 mV and 27 mV, respectively. While the overpotentials of Rh NPs and RhNi NPs are 80 mV and 46 mV, respectively. These results manifest that 2D nanosheets display better catalytic activities compared to nanoparticles in acidic media. We propose that the improvement of activity can be attributed to the advantages of hierarchical ultrathin nanosheets, which provided more active sites and promoted electron transfer.^{23,38,47} Meanwhile, the RhNi NSs present a superior HER performance to the monometallic Rh NSs, indicating that alloying effect might enhance the activity of catalyst due to the modified electronic structure and adsorption energy.^{42,45,49}

In addition, Tafel slope plays a vital role in assessing the reaction kinetics for water splitting. The corresponding Tafel

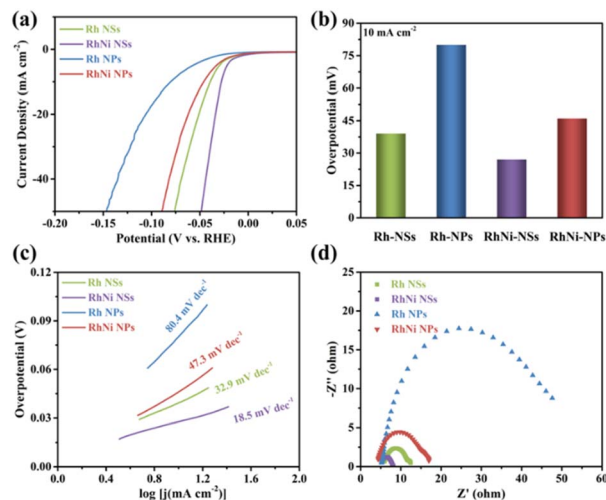


Fig. 4 HER performances of Rh NSs, RhNi NSs, Rh NPs and RhNi NPs in 0.5 M H_2SO_4 electrolyte. (a) HER polarization curves, (b) required overpotentials at 10 mA cm^{-2} , (c) Tafel plots obtained from the corresponding polarization curves, and (d) corresponding Nyquist Plots.

plots were obtained from the fitted LSV curves. As shown in Fig. 4c, the Tafel slopes for Rh NSs, RhNi NSs, Rh NPs and RhNi NPs are 32.9 mV dec^{-1} , 18.5 mV dec^{-1} , 80.4 mV dec^{-1} and 47.3 mV dec^{-1} , respectively. As expected, the catalysts of Rh NSs and RhNi NSs present smaller Tafel slopes, indicating the better catalytic activity as well as faster catalytic kinetics of the HER process. Apparently, the HER processes on Rh NSs and RhNi NSs undergo the Volmer–Tafel mechanism, which confirms that the structure of hierarchical ultrathin nanosheets and the design of alloy can substantially improve the HER kinetics.

Furthermore, Rh NSs and RhNi NSs have larger peak area for underpotentially deposited hydrogen (H_{upd}) compared to Rh NPs and RhNi NPs in cyclic voltammograms (CV) (Fig. S7†), demonstrating that the ultrathin nanosheets structure might provide more catalytic active sites. The electrochemically active surface areas (ECSAs) of the prepared electrocatalysts are further evaluated by the double layer capacitance (C_{dl}) (Fig. S8†), which is obtained by calculating CV curves in a non-faradaic region under different scan rates (20 to 120 mV s^{-1}). As displayed in Fig. S8e,† Rh NSs and RhNi NSs possess higher C_{dl} value compared to Rh NPs and RhNi NPs, due to the advantages of 2D nanosheets structure with more active reaction sites.^{24–28}

To understand the charge transfer kinetics of electrocatalysts, electrochemical impedance spectroscopy (EIS) tests were also carried out on Rh NSs, RhNi NSs, Rh NPs and RhNi NPs respectively. As shown in Fig. 4d, the Nyquist plots of Rh NSs and RhNi NSs indicate that Rh NSs and RhNi NSs have smaller charge transfer resistances (R_{ct}), which are in agreement with that of the overpotential and the Tafel slope, indicating that the unique structure and alloy can substantially accelerate the interfacial electron-transfer kinetics.

Except for the catalytic activity, the long-term stability and durability of HER electrocatalysts are also important factors in achieving effective water splitting. The long-term stability of electrocatalysts was assessed by 1000 CV tests in 0.5 M H_2SO_4



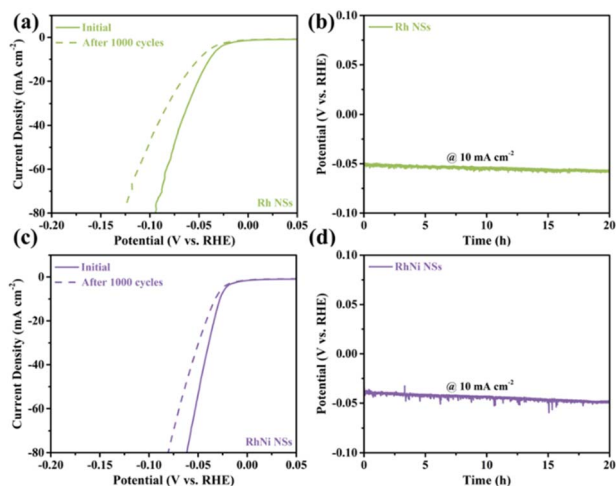


Fig. 5 HER polarization curves of (a) Rh NSs and (c) RhNi NSs electrocatalysts before and after 1000 CV cycles. Chronopotentiometry (V–t) curves of (b) Rh NSs and (d) RhNi NSs at a constant current density of 10 mA cm⁻².

electrolyte. The LSV polarization curves of Rh NSs and RhNi NSs display slight decrease after 1000 cycles (Fig. 5a and c), whereas the LSV polarization curves of Rh NPs and RhNi NPs show significant decrease (Fig. S9a and c†). The durability of electrocatalysts was assessed by chronopotentiometry at a constant current density of 10 mA cm⁻². After 20 h of durability testing, the overpotentials of the Rh NSs and RhNi NSs remain slightly changed (Fig. 5b and d), while the Rh NPs and RhNi NPs present a large variation (Fig. S9b and d†). The better catalytic stability and durability might be attributed to the rapid diffusion of reactants and interfacial charge transfer provided by nanosheets morphology. Besides, the hierarchical architecture assembled by ultrathin nanosheets can prevent the agglomeration of electrocatalysts, which could also improve the catalytic and structural stability of catalyst.

Conclusions

In conclusion, we report a facile urea-mediated route for the preparation of hierarchical ultrathin Rh-based nanosheets without involving of toxic chemicals as structure-directing agents. The advantages of structure impart Rh NSs and RhNi NSs catalysts with higher HER activity, which significantly surpasses that of Rh NPs and RhNi NPs. This work may provide an important reference to construct 2D noble metal catalysts for highly active electrocatalytic performance.

Conflicts of interest

There are no conflicts of interest to declare.

Acknowledgements

This work was supported by the Guangdong Basic and Applied Basic Research Foundation (2020A1515110120), Innovation

Foundation of Educational Commission of Guangdong Province (2020KQNCX090), Basic and Applied Basic Research Foundation of Jiangmen (2020030102940008548), and Science Foundation of High-Level Talents of Wuyi University (2019AL029, 2021AL019).

Notes and references

- 1 J.-S. Li, J.-Y. Li, M.-J. Huang, L.-X. Kong and Z. Wu, *Carbon*, 2020, **161**, 44–50.
- 2 W. Li, Y. Zhao, Y. Liu, M. Sun, G. I. N. Waterhouse, B. Huang, K. Zhang, T. Zhang and S. Lu, *Angew. Chem.*, 2021, **60**, 3290–3298.
- 3 J. Shan, T. Ling, K. Davey, Y. Zheng and S. Z. Qiao, *Adv. Mater.*, 2019, **31**(17), 1900510.
- 4 J. N. Tiwari, S. Sultan, C. W. Myung, T. Yoon, N. Li, M. Ha, A. M. Harzandi, H. J. Park, D. Y. Kim, S. S. Chandrasekaran, W. G. Lee, V. Vij, H. Kang, T. J. Shin, H. S. Shin, G. Lee, Z. Lee and K. S. Kim, *Nat. Energy*, 2018, **3**, 773–782.
- 5 Y. Yang, Y. Yu, J. Li, Q. Chen, Y. Du, P. Rao, R. Li, C. Jia, Z. Kang, P. Deng, Y. Shen and X. Tian, *Nanomicro Lett.*, 2021, **13**, 160.
- 6 Z. Chen, X. Duan, W. Wei, S. Wang and B.-J. Ni, *Nano Energy*, 2020, **78**, 105270.
- 7 L. Li, P. Wang, Q. Shao and X. Huang, *Chem. Soc. Rev.*, 2020, **49**, 3072–3106.
- 8 L. Peng, C. Wang, Q. Wang, R. Shi, T. Zhang and G. I. N. Waterhouse, *Adv. Energy Sustainability Res.*, 2021, **2**, 2100078.
- 9 Y. Xu, M. Liu, M. Wang, T. Ren, K. Ren, Z. Wang, X. Li, L. Wang and H. Wang, *Appl. Catal., B*, 2022, **300**, 120753.
- 10 Y. Yao, Z. Zhang and L. Jiao, *Energy Environ. Mater.*, 2021, **5**, 470–485.
- 11 S. Chen, C. Lv, L. Liu, M. Li, J. Liu, J. Ma, P. Hao, X. Wang, W. Ding, M. Xie and X. Guo, *J. Energy Chem.*, 2021, **59**, 212–219.
- 12 Y. Jiang, M. Yang, M. Qu, Y. Wang, Z. Yang, Q. Feng, X. Deng, W. Shen, M. Li and R. He, *J. Mater. Chem. A*, 2020, **8**, 10409–10418.
- 13 S. Y. Pang, W. F. Io and J. Hao, *Adv. Sci.*, 2021, **8**, e2102207.
- 14 S. Yin, Z. Wang, H. Zhang, C. Li, H. Yu, Y. Xu, X. Li, L. Wang and H. Wang, *Chem. Eng. J.*, 2020, **399**, 2010072.
- 15 W. Zhang, B. Huang, K. Wang, W. Yang, F. Lv, N. Li, Y. Chao, P. Zhou, Y. Yang, Y. Li, J. Zhou, W. Zhang, Y. Du, D. Su and S. Guo, *Adv. Energy Mater.*, 2020, **11**, 2003192.
- 16 J. Du, X. Wang, C. Li, X.-Y. Liu, L. Gu and H.-P. Liang, *Electrochim. Acta*, 2018, **282**, 853–859.
- 17 J. Kim, K. Kani, J. Kim, J. S. Yeon, M.-K. Song, B. Jiang, J. Na, Y. Yamauchi and H. S. Park, *J. Ind. Eng. Chem.*, 2021, **96**, 371–375.
- 18 Q. Mao, S. Jiao, K. Ren, S. Wang, Y. Xu, Z. Wang, X. Li, L. Wang and H. Wang, *Chem. Eng. J.*, 2021, **426**, 131227.
- 19 X. Mu, J. Gu, F. Feng, Z. Xiao, C. Chen, S. Liu and S. Mu, *Adv. Sci.*, 2021, **8**, 2002341.



- 20 H. Wang, S. Jiao, S. Liu, S. Wang, T. Zhou, Y. Xu, X. Li, Z. Wang and L. Wang, *ACS Appl. Mater. Interfaces*, 2021, **13**, 30479–30485.
- 21 A. Yu, S. Y. Kim, C. Lee, M. H. Kim and Y. Lee, *ACS Appl. Mater. Interfaces*, 2019, **11**, 46886–46893.
- 22 H. Zhang, S. Liu, P. Tian, Y. Mao, Y. Xu, H. Wang, X. Li, Z. Wang and L. Wang, *Chem. Eng. J.*, 2022, **435**, 134798.
- 23 Y. Zhao, N. Jia, X.-R. Wu, F.-M. Li, P. Chen, P.-J. Jin, S. Yin and Y. Chen, *Appl. Catal., B*, 2020, **270**, 118880.
- 24 Z. Lin, B. Xiao, Z. Wang, W. Tao, S. Shen, L. Huang, J. Zhang, F. Meng, Q. Zhang, L. Gu and W. Zhong, *Adv. Funct. Mater.*, 2021, **31**, 2102321.
- 25 X. Mu, X. Gu, R. Zhou, L. Li, G. Lu, C. Chen, S. Liu, S. Mu and W. Chen, *Chem. Eng. J.*, 2022, **428**, 131099.
- 26 J. Xu and X. Kong, *Small Methods*, 2022, **6**, e2101432.
- 27 J. Yang, L. Xu, W. Zhu, M. Xie, F. Liao, T. Cheng, Z. Kang and M. Shao, *J. Mater. Chem. A*, 2022, **10**, 1891–1898.
- 28 Y. Zhao, H. Cong, P. Li, D. Wu, S. Chen and W. Luo, *Angew. Chem.*, 2021, **60**, 7013–7017.
- 29 Q.-L. Hong, Q.-G. Zhai, X.-L. Liang, Y. Yang, F.-M. Li, Y.-C. Jiang, M.-C. Hu, S.-N. Li and Y. Chen, *J. Mater. Chem. A*, 2021, **9**, 3297–3302.
- 30 D. Weber, L. M. Schoop, D. Wurmbbrand, S. Laha, F. Podjaski, V. Duppel, K. Müller, U. Starke and B. V. Lotsch, *J. Mater. Chem. A*, 2018, **6**, 21558–21566.
- 31 L. Zhuang, L. Ge, Y. Yang, M. Li, Y. Jia, X. Yao and Z. Zhu, *Adv. Mater.*, 2017, **29**, 1606793.
- 32 J. Wu, X. Cui, J. Fan, J. Zhao, Q. Zhang, G. Jia, Q. Wu, D. Zhang, C. Hou, S. Xu, D. Jiao, L. Gu, D. J. Singh and W. Zheng, *ACS Energy Lett.*, 2021, **6**, 1912–1919.
- 33 J.-Y. Zhu, S. Chen, Q. Xue, F.-M. Li, H.-C. Yao, L. Xu and Y. Chen, *Appl. Catal., B*, 2020, **264**, 118520.
- 34 Q. Chen, Z. Chen, A. Ali, Y. Luo, H. Feng, Y. Luo, P. Tsiakaras and P. Kang Shen, *Chem. Eng. J.*, 2022, **427**, 131565.
- 35 J. Jiang, S. Lu, H. Gao, X. Zhang and H.-Q. Yu, *Nano Energy*, 2016, **27**, 526–534.
- 36 M. Wei, L. Huang, L. Li, F. Ai, J. Su and J. Wang, *ACS Catal.*, 2022, **12**, 6478–6485.
- 37 Q. Yang, L. Shi, B. Yu, J. Xu, C. Wei, Y. Wang and H. Chen, *J. Mater. Chem. A*, 2019, **7**, 18846–18851.
- 38 Y. Zhao, J. Bai, X.-R. Wu, P. Chen, P.-J. Jin, H.-C. Yao and Y. Chen, *J. Mater. Chem. A*, 2019, **7**, 16437–16446.
- 39 J. Ge, P. Yin, Y. Chen, H. Cheng, J. Liu, B. Chen, C. Tan, P. F. Yin, H. X. Zheng, Q. Q. Li, S. Chen, W. Xu, X. Wang, G. Wu, R. Sun, X. H. Shan, X. Hong and H. Zhang, *Adv. Mater.*, 2021, **33**, e2006711.
- 40 J. Fan, J. Wu, X. Cui, L. Gu, Q. Zhang, F. Meng, B. H. Lei, D. J. Singh and W. Zheng, *J. Am. Chem. Soc.*, 2020, **142**, 3645–3651.
- 41 M. Luo, Z. Zhao, Y. Zhang, Y. Sun, Y. Xing, F. Lv, Y. Yang, X. Zhang, S. Hwang, Y. Qin, J. Y. Ma, F. Lin, D. Su, G. Lu and S. Guo, *Nature*, 2019, **574**, 81–85.
- 42 G. Liu, W. Zhou, B. Chen, Q. Zhang, X. Cui, B. Li, Z. Lai, Y. Chen, Z. Zhang, L. Gu and H. Zhang, *Nano energy*, 2019, **66**, 104173.
- 43 H. Duan, N. Yan, R. Yu, C. R. Chang, G. Zhou, H. S. Hu, H. Rong, Z. Niu, J. Mao, H. Asakura, T. Tanaka, P. J. Dyson, J. Li and Y. Li, *Nat. Commun.*, 2014, **5**, 3093.
- 44 J. Fan, X. Cui, S. Yu, L. Gu, Q. Zhang, F. Meng, Z. Peng, L. Ma, J. Y. Ma, K. Qi, Q. Bao and W. Zheng, *ACS Nano*, 2019, **13**, 12987–12995.
- 45 D. Cao, H. Xu and D. Cheng, *Adv. Energy Mater.*, 2020, **10**, 1903038.
- 46 X. Fu, Z. Zhao, C. Wan, Y. Wang, Z. Fan, F. Song, B. Cao, M. Li, W. Xue, Y. Huang and X. Duan, *Nano Res.*, 2018, **12**, 211–215.
- 47 Y. Zhao, S. Xing, X. Meng, J. Zeng, S. Yin, X. Li and Y. Chen, *Nanoscale*, 2019, **11**, 9319–9326.
- 48 L. Sahoo, R. Garg, K. Kaur, C. P. Vinod and U. K. Gautam, *Nano Lett.*, 2022, **22**, 246–254.
- 49 L. Fu, X. Zeng, G. Cheng and W. Luo, *ACS Appl. Mater. Interfaces*, 2018, **10**, 24993–24998.

